The Astrophysical Journal, 715:1302–1317, 2010 June 1 doi:10.1088/0004-637X/715/2/1302

MOLECULAR CLOUD EVOLUTION. III. ACCRETION VERSUS STELLAR FEEDBACK

Enrique Vázquez-Semadeni, Pedro Colín, Gilberto C. Gómez, Javier Ballesteros-Paredes, and Alan W. Watson[1]
Centro de Radioastronomía y Astrofísica, Universidad Nacional Autónoma de México, Campus Morelia, Apdo. Postal 3-72, Morelia 58089, Mexico;
e.vazquez@crya.unam.mx, p.colin@crya.unam.mx, g.gomez@crya.unam.mx, alan@astro.unam.mx
Received 2009 December 12; accepted 2010 March 30; published 2010 May 10

ABSTRACT

We numerically investigate the effect of feedback from the ionization heating from massive stars on the evolution of giant molecular clouds (GMCs) and their star formation efficiency (SFE), which we treat as an instantaneous, time-dependent quantity. We follow the GMCs' evolution from their formation to advanced star-forming stages. After an initial period of contraction, the collapsing clouds begin forming stars, whose feedback evaporates part of the clouds' mass, opposing the continuing accretion from the infalling gas. Our results are as follows: (1) in the presence of feedback, the clouds attain levels of the SFE that are consistent *at all times* with observational determinations for regions of comparable star formation rates. (2) However, the dense gas mass is *larger* in general in the presence of feedback, while the total mass (dense gas + stars) is nearly insensitive to the presence of feedback, suggesting that it is determined mainly by the accretion, while the feedback inhibits mainly the conversion of dense gas to stars, because it acts directly to reheat and disperse the gas that is directly on its way to forming stars. (3) The factor by which the SFE is reduced upon the inclusion of feedback is a decreasing function of the cloud's mass, for clouds of size ∼10 pc. This naturally explains the larger observed SFEs of massive-star-forming regions. (4) The clouds may attain a pseudo-virialized state, with a value of the virial mass very similar to the actual cloud mass. However, this state differs from true virialization in that the clouds, rather than being equilibrium entities, are the centers of a larger-scale collapse, in which accretion replenishes the mass consumed by star formation. (5) The higher-density regions within the clouds are in a similar situation, accreting gas infalling from the less-dense, more extended regions of the clouds. (6) The density probability density functions of the regions containing the clouds in general exhibit a shape characteristic of thermally bistable flows, and extend down to densities corresponding to the warm atomic medium, because the warm gas interpenetrates the clouds. The general picture arising from our simulations is that the gas involved in the gravitational contraction leading to star formation extends to large scales and is not confined to the local environment of the final collapse, where the effect of the feedback is active, in agreement with recent proposals of a gravitationally driven mass cascade from large to small scales.

Key words: H II regions – ISM: clouds – stars: formation – turbulence

Online-only material: color figures, animations

1. INTRODUCTION

The evolution of giant molecular clouds (GMCs) is a key ingredient in our understanding of the star formation process. In particular, the low observed star formation efficiency (SFE) at the scale of whole GMCs (∼2%; Myers et al. 1986) remains a topic of strong debate, with there being two main competing scenarios that attempt to explain it, within the framework of a turbulent control of star formation (Mac Low & Klessen 2004). These scenarios refer essentially to the effect of the stellar feedback (mainly from massive stars) on the star-forming clouds. One is the scenario that the stars quickly disrupt their parent clouds by dispersal and/or photoionization, before the gaseous mass of the cloud is completely converted to stars (e.g., Whitworth 1979; Elmegreen 1983; Franco et al. 1994; Williams & McKee 1997; Hartmann et al. 2001). In this case, the star formation rate (SFR) of active star-forming sites may be large for brief periods and then halted by the very stars that have just been formed.

In the other scenario, the role of stellar feedback is to drive turbulent motions within the GMC, which opposes its self-gravity, allowing it to remain in near stationary equilibrium for times significantly longer than its free-fall time ($t_{\rm ff}$; Norman & Silk 1980; Krumholz & McKee 2005; Krumholz et al. 2006; Li & Nakamura 2006). In this case, the low efficiency of star formation would be due to the dual role of supersonic turbulence in self-gravitating clouds, of opposing global collapse of the cloud while promoting local collapse of turbulent density enhancements, which involve small fractions of the total cloud mass (Klessen et al. 2000; Vázquez-Semadeni et al. 2003; see also the reviews by Mac Low & Klessen 2004; Ballesteros-Paredes et al. 2007).

Another controversy, related to the control of the SFE, refers to the nature of the motions originating the line widths observed in GMCs and their substructures. The latter were initially proposed to correspond to gravitational contraction by Goldreich & Kwan (1974), but this suggestion was quickly deemed untenable by Zuckerman & Palmer (1974), who noted that it would imply total Galactic SFRs of the order of the total molecular gas mass in the Galaxy ($\sim 10^9\ M_\odot$) divided by the typical free-fall time for a GMC (∼4 Myr), or $\sim 250\ M_\odot\ {\rm yr}^{-1}$, an estimate roughly 2 orders of magnitude larger than the observed Galactic SFR. Zuckerman & Evans (1974) then suggested that the observed line widths could correspond instead to random, small-scale[2] turbulent motions, a notion that has prevailed until the present. However, a number of workers have recently advocated a return to the gravitational contraction picture, noting that various observational properties of clouds and clumps

[1] Also at Instituto de Astronomía, Universidad Nacional Autónoma de México, A.P. 70-264, 04510, México, D.F., Mexico.

[2] Zuckerman & Evans (1974) referred to these motions as "local," and explicitly discarded large-scale coherent motions such as gravitational contraction.

can be well matched by models dominated by gravitational contraction (e.g., Hartmann & Burkert 2007; Peretto et al. 2007; Vázquez-Semadeni et al. 2009). Moreover, the notion of completely random, small-scale turbulent motions appears difficult to reconcile with the recent realization that the principal component of the velocity differences within clouds and clumps at all scales appears to be "dipolar," indicative of coherent motions at the scale of the whole cloud or clump (Heyer & Brunt 2007; Brunt et al. 2009). In general, several studies comparing simulations and observations have concluded that the motions in molecular clouds are consistent with large-, rather than small-scale driving (Ossenkopf & Mac Low 2002; Brunt 2003; Padoan et al. 2009).

If a return to the collapsing scenario is to be considered, it is necessary to somehow avoid the Zuckerman & Palmer (1974) criticism of it. This is actually not so difficult because that criticism neglects the internal structure of the GMCs. Recent numerical studies of cloud formation by converging streams of warm neutral gas in the interstellar medium show that the clouds are born turbulent, due to one or more of the thermal, thin-shell, and Kelvin–Helmholz instabilities (Hennebelle & Pérault 1999; Koyama & Inutsuka 2000, 2002; Audit & Hennebelle 2005; Heitsch et al. 2005; Vázquez-Semadeni et al. 2006). The turbulence is subsonic with respect to the warm gas, but supersonic with respect to the cold phase, implying large density fluctuations in the latter. In fact, it has recently been proposed that molecular clouds may actually contain a warmer, atomic substrate in which colder molecular clumps are embedded (Hennebelle & Inutsuka 2006). In either case, the molecular cloud contains large, *nonlinear* density enhancements in which the local free-fall time is significantly shorter than the cloud's average. Thus, once the global collapse begins, the local clumps may complete their collapses earlier than the bulk of the cloud. They can thus begin forming stars that can begin their feedback action on the GMC before it completes the bulk collapse.

In this paper, we present numerical simulations aimed at investigating this scenario, in which we use the same cloud formation setup of previous papers (Vázquez-Semadeni et al. 2007, hereafter Paper I; Banerjee et al. 2009), but including a prescription for stellar feedback mimicking ionization heating from massive stars. With this tool, we investigate the effect of the feedback on the global SFE of the evolving GMC, as well as the nature of the motions in the cloud, in a first effort to shed light on these issues. As we shall see, it turns out that the physical conditions in the clouds differ significantly from the "normal" picture, since accretion of gas from the warm diffuse medium is an integral part of the clouds' dynamics and evolution, and thus the clouds cannot be considered as isolated.

The plan of the paper is as follows. In Section 2, we describe the numerical code, and the implementation of our star formation and stellar feedback prescriptions. In Section 3, we describe the simulations, and in Section 4 we describe the results concerning the control of the SFE by stellar feedback and the nature of the "clouds" themselves. Finally, in Section 6 we present a summary and some conclusions.

2. THE NUMERICAL MODEL

2.1. Heating and Cooling

The numerical simulations used in this work were performed using the hydrodynamics + N-body adaptive refinement tree (ART) code (Kravtsov et al. 1997; Kravtsov 2003). Among the physical processes implemented in ART, relevant for our physical problem are the radiative heating and cooling of the gas, its conversion into stars, ionization-like heating from stellar feedback, and self-gravity, from both the stars and the gas.

We use heating (Γ) and cooling (Λ) functions of the form

$$\Gamma = 2.0 \times 10^{-26} \text{ erg s}^{-1} \tag{1}$$

$$\frac{\Lambda(T)}{\Gamma} = 10^7 \exp\left(\frac{-1.184 \times 10^5}{T + 1000}\right) + 1.4 \times 10^{-2}\sqrt{T} \exp\left(\frac{-92}{T}\right) \text{ cm}^3. \tag{2}$$

These functions are fits to the various heating and cooling processes considered by Koyama & Inutsuka (2000), as given by Equation (4) of Koyama & Inutsuka (2002).[3] With these heating and cooling laws, the gas is thermally unstable in the density range 1 cm$^{-3} \lesssim n \lesssim 10$ cm^{-3} (cf. Paper I).

2.2. Star Formation and Stellar Feedback Prescriptions

In ART, star formation is modeled as taking place in the densest regions, defined by $n > n_{\rm SF}$, where n is the local number density of the gas and $n_{\rm SF}$ is a density threshold. A stellar particle of mass m_* is placed in a grid cell where this condition is satisfied, and this mass is removed from the gas mass in the cell. Thereafter, the particle is treated as non-collisional, and follows N-body dynamics. No other criteria are imposed. In each gas cell that satisfies the above criteria, a stellar particle is formed with a mass equal to 50% of the gas mass contained in the cell. Since the stellar particles are more massive than a single star, each stellar particle should be considered as a small cluster, within which the individual stellar masses are distributed according to some stellar initial mass function (IMF).

Stellar particles inject thermal energy at a rate $\dot{E}$ per particle. The energy is deposited in the cell in which the stellar particle is instantaneously located, and we keep the energy injection on over a typical OB stellar lifetime, which we assume to be 10 Myr. It is important to note that, although initially we experimented with realistic values of $\dot{E}$ based on the Lyman continuum fluxes of stars with masses between 10 and 20 $M_\odot$ (e.g., Diaz-Miller et al. 1998), we found that, because all the energy is deposited in a single cell, and the neighboring cells are heated exclusively by conduction, rather than by radiative heating, the resulting H II regions were not so realistic. Thus, we opted instead for taking $\dot{E}$ as a free parameter, and adjusting it until we obtained realistic H II regions, with temperatures $\sim 10^4$ K, diameters of a few parsecs, and expansion velocities of a few tens of km s^{-1}.

Note also that we resort to the common strategy of turning off the cooling in the cell where a stellar particle is located, so that the cell can reach realistically high temperatures. Otherwise, the cooling can dissipate most of the thermal energy deposited in very dense cells. In the real ISM, this does not occur because the stellar heating is applied through ionization, so that the temperature reached in the star's immediate environment is independent of the medium's local density. Instead, in the simulations, the cooling depends on the density, and the temperature resulting from the balance between the stellar heating and the cooling does depend on the density. This problem is avoided by turning off the cooling in the cell

[3] As noted in Paper I, Equation (4) in Koyama & Inutsuka (2002) contains two typographical errors. The form used here incorporates the necessary corrections, kindly provided by H. Koyama (2007, private communication).

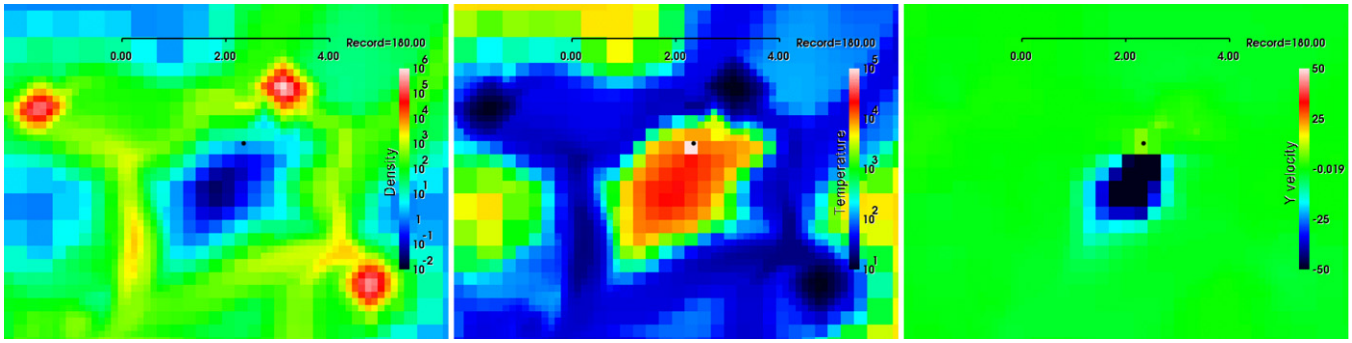

Figure 1. Cross sections of the density (left panel), temperature (middle panel), and y-speed (right panel), shown on the x–z plane, of a typical isolated H II region. The scale bar near the top indicates length in parsecs.

(A color version of this figure is available in the online journal.)

where the stellar particle is located. Note that this contradicts claims that the need to turn off the cooling can be alleviated simply by increasing the resolution (e.g., Ceverino & Klypin 2009). We argue that this problem can only be alleviated by performing radiation-hydrodynamics simulations. In their absence, we consider that turning off the cooling is actually a *better* model of the effect of stellar feedback, because it allows mimicking the fact that the gas temperature in the H II regions is independent of the local density.

Finally, in order to further constrain the physical conditions in the H II regions, we also impose a "ceiling" to the temperature in the cell containing the stellar particle because otherwise, with the cooling off, the temperature in the cell might diverge. We set this "ceiling" to 10^6 K.

Although this procedure is mostly one of trial and error, we consider it to be the most adequate one for our purposes, since it is the H II regions that drive the turbulent motions in the dense gas in our simulations, and so it is them that must have realistic properties, even at the expense of a somewhat ad hoc star formation prescription. We show a typical H II region in our simulation in Figure 1.

2.3. Refinement

The numerical box is initially covered by a grid of 128^3 (zeroth level) cells. The mesh is subsequently refined as the matter distribution evolves. The maximum allowed refinement level was set to four, so that high-density regions have an effective resolution of 2048^3 cells, with a minimum cell size of 0.125 pc. Cells are refined (halved in linear size) if the gas mass within the cell is greater than 0.32 $M_\odot$. That is, the cell is refined by a factor of 2 when the density increases by a factor of 8, so that, while refinement is active, the grid cell size Δx scales with density n as $\Delta x \propto n^{-1/3}$. Once the maximum refinement level is reached, no further refinement is performed, and the cell's mass can reach much larger values. In particular, a stellar particle is formed when a fourth-level cell reaches a density $n_{\rm SF} = 4 \times 10^6$ cm^{-3}, or a mass of 243.5 $M_\odot$, again assuming $\mu = 1.27$ (we use this value because we do not follow the actual chemistry, and thus we assume the entire box to be filled with atomic hydrogen.) Thus, a stellar particle typically has a mass $\gtrsim$122 $M_\odot$.

Note that, because we use only four levels of refinement, the largest densities arising in the simulation are by far not sufficiently resolved according to the "Jeans criterion" proposed by Truelove et al. (1997) for adaptive-mesh codes. Specifically, at our stellar-particle formation threshold density of 4×10^6 cm^{-3}, and assuming a gas temperature of $T \sim 15$ K at that density, we find that the Jeans length (using the adiabatic sound speed) is $\sim$0.031 pc, while the minimum cell size, at 0.125 pc, is roughly 4 times larger. Thus, according to those authors, one should expect artificial fragmentation to occur in our simulations. However, we do not consider this to be a problem because we are not concerned here with the numbers and masses of the stellar particles formed in the simulation, but simply with the *total* amount of mass that goes into stars.

3. THE SIMULATIONS

We consider four simulations using the same setup as in Paper I, which represents the evolution of a region of 256 pc per side, initially filled with warm gas at a uniform density of $n_0 = 1$ cm^{-3} and a temperature of $T_0 = 5000$ K, implying an adiabatic sound speed $c_{\rm s} = 7.4$ km s^{-1} (assuming a mean particle mass $\mu = 1.27$). The whole numerical box thus contains 5.25×10^5 $M_\odot$. In this medium, we set up two streams moving with the same speed $v_{\rm inf} = 5.9$ km s^{-1} (corresponding to a Mach number of 0.8 with respect to the unperturbed medium) in opposite senses along the x-direction. The streams have a radius of 32 pc and a length of 112 pc each, so that the total mass in the two inflows is 2.25×10^4 $M_\odot$. The flows collide head on at the box's center (see Figure 1 of Paper I). To the inflow velocity field we superpose a field of initial low-amplitude turbulent velocity fluctuations, in order to trigger the instabilities in the compressed layer. We create this initial velocity fluctuation field with a new version of the spectral code used in Vazquez-Semadeni et al. (1995) and Passot et al. (1995), modified to run in parallel in shared-memory architectures. The simulations are evolved for about 40 Myr.

The collision nonlinearly triggers a phase transition to the cold neutral medium, forming a turbulent, cold, dense cloud (Audit & Hennebelle 2005; Heitsch et al. 2005, 2006; Vázquez-Semadeni et al. 2006), consisting of a complex network of sheets, filaments, and clumps of cold gas embedded in a warm diffuse substrate (Audit & Hennebelle 2005; Hennebelle & Inutsuka 2006; Hennebelle & Audit 2007). The largest cold structures may become gravitationally unstable and begin to collapse. Eventually, they proceed to forming stars, which then heat their environment, forming expanding "H II regions" that tend to disperse the clumps.

In the simulations reported here, we vary only two parameters: the amplitude of the initial velocity fluctuations, and whether the stellar feedback is on or off. We consider a "large-amplitude" (LA) and a "small-amplitude" (SA) case for the initial velocity fluctuations, for which the three-dimensional velocity

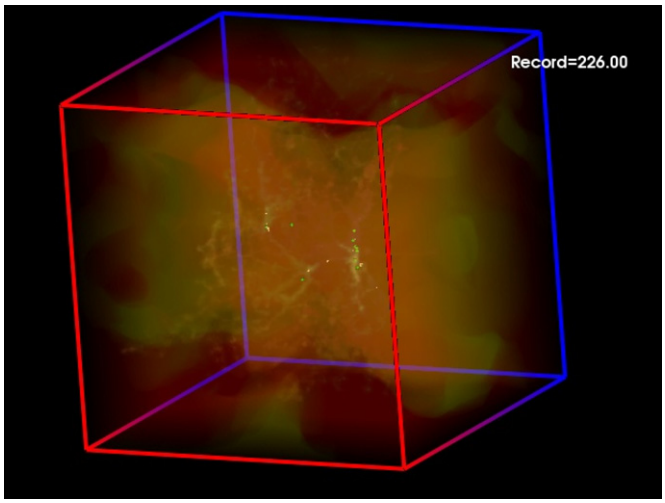

Figure 2. View in projection of the whole numerical box for simulation LAF1 at $t \approx 31.64$ Myr. The box size is 256 pc. The green dots indicate stellar particles. The light yellow spots are transient dense cores, highlighted by saturation of the color table. In the online version, this figure shows an animation of the entire evolution of the simulation up to $t = 40$ Myr. Records are spaced by a time interval $\Delta t \approx 0.14$ Myr.
(A color version and an animation of this figure are available in the online journal.)

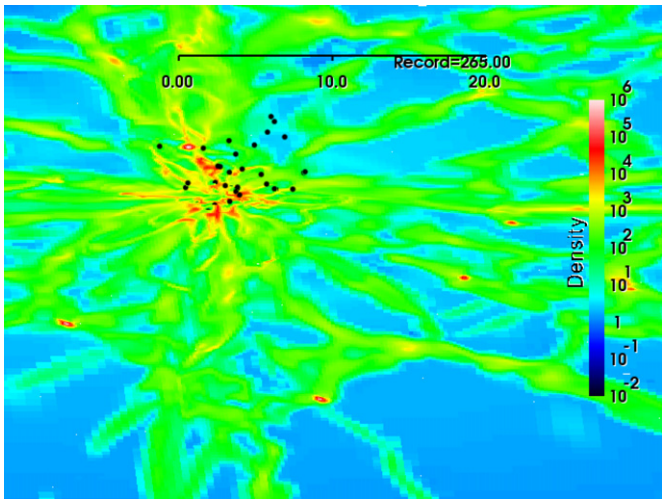

Figure 3. Cross-sectional view through the Central Cloud in run SAF1 at $t \approx 33$ Myr, at which time it has grown to a mass of $\sim 3 \times 10^4\ M_\odot$. The plane of the image is shown from an inclined line of sight for better perspective. The cloud is seen to contain numerous H II regions mixed with dense regions. In the online version, this figure shows an animation of the buildup of this cloud, illustrating how it forms by the continued accretion of infalling material from the globally collapsing GMC. In the animation, note that many of the infalling clumps form stellar particles before reaching the center and are disrupted by the local stellar feedback. However, once the Central Cloud is fully assembled, it resists dispersal and forms stars at a high rate.
(A color version and an animation of this figure are available in the online journal.)

Table 1
Run Parameters

Run Name	$v_{\rm rms}$ (km s^{-1})	Feedback
LAF0	1.7	Off
LAF1	1.7	On
SAF0	0.1	Off
SAF1	0.1	On

dispersions are $v_{\rm rms} \sim 1.7$ km s^{-1} and $v_{\rm rms} \sim 0.1$ km s^{-1}, respectively. We thus employ a mnemonic nomenclature for the runs using the acronyms LA or SA, followed by F0 or F1, indicating that feedback is off or on, respectively. Table 1 summarizes the runs considered in the paper.

4. RESULTS

4.1. Evolution of the Simulations

The simulations performed here behave very similarly to previous simulations with similar setups, performed with other codes. In particular, our SA runs are very similar to run L256Δv0.17 in Paper I and the run presented by Banerjee et al. (2009). The main feature of these runs is that, because the initial fluctuations are very mild, the flow collision creates a large, coherent "pancake" of cold, dense gas, which is able to undergo gravitational collapse as a whole. This results in the formation of a dense, massive, and turbulent region at the site where the global collapse finally converges, with physical properties similar to those of high-mass star-forming regions (Vázquez-Semadeni et al. 2009). However, a recent study varying the parameters of the flow collision (Rosas-Guevara et al. 2010) shows that the coherence of the collapse may be lost in the presence of stronger initial velocity fluctuations, and the SFE is decreased. In such cases, smaller clouds appeared to be less strongly gravitationally bound, with the effect of decreasing the SFE. This feature also happens in our LA simulations, in which the cloud formed by the initial flow is much more fragmented and scattered over the simulation volume. As a result, star formation also occurs in a much more scattered manner, and the SFEs are in general smaller in the LA runs than in their SA counterparts.

However, in general a common pattern is followed by all simulations: the transonic converging flows in the diffuse gas induce a phase transition to the cold phase of the atomic gas, which is highly prone to gravitational instability. This can be seen as follows. The thermal pressure at our initial conditions is 5000 K cm^{-3}. From Figure 2 of Paper I, it can be seen that the thermal balance conditions of the cold medium at that pressure are $n \sim 130$ cm^{-3}, $T \sim 40$ K. At these values, the Jeans length and mass are $\sim$7 pc and $\sim$640 $M_\odot$, respectively. These sizes and masses are easily achievable by a large fraction of the cold gas structures, which can then proceed to gravitational collapse and form stars. Moreover, the ensemble of these clumps may also be gravitationally unstable as a whole, the likelihood of this being larger for greater coherence of the large-scale pattern.

Regions of active star formation form in both sets of simulations by the gravitational merging of pre-existing smaller-scale clumps, which, altogether, form a larger-scale GMC. Figure 2 shows a whole-box image of the density field in run LAF1, in projection. In the online version of the paper, this figure shows an animation of this run from $t = 0$ to $t \approx 40$ Myr, illustrating the entire evolution of the simulation, from the assembly of the cloud to its advanced star-forming epochs. In the animation, subsequent "records" are separated by time intervals $\Delta t \approx 0.14$ Myr.

In the SA runs, the largest star-forming region forms in the center of the numerical box, due to the coherent collapse of the entire sheet-like cloud formed by the collision. This was the region shown in Vázquez-Semadeni et al. (2009) to exhibit physical conditions typical of actual high-mass star-forming regions. We refer to this region as "the Central Cloud." Figure 3 shows a view of this region at $t \approx 33$ Myr, a time at which the

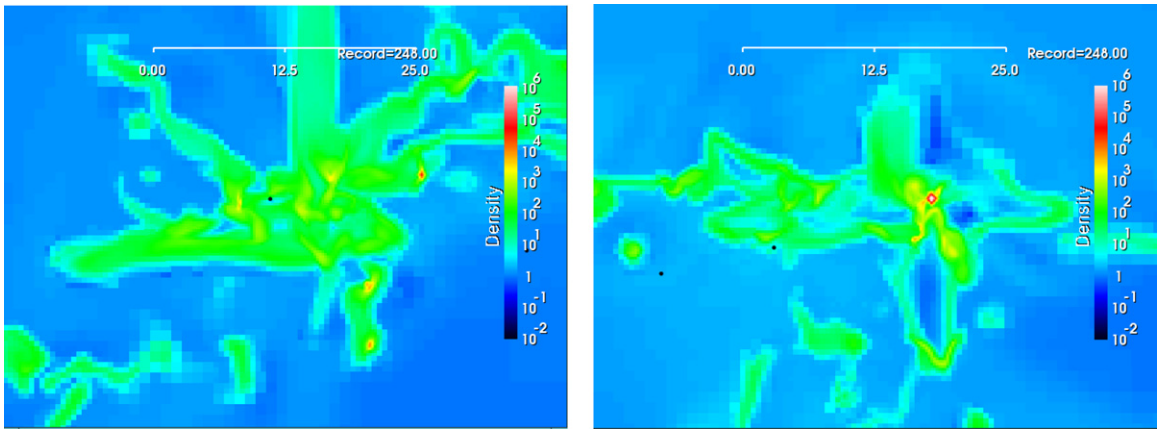

Figure 4. Cross-sectional view through Clouds 1 (left panel) and 2 (right panel) at $t \sim 35$ Myr in simulation LAF1. The plane of view is located at $x = 100$ pc for Cloud 1 and at $x = 150$ pc for Cloud 2. The dots represent the stellar particles. In the online version, these figures show animations of the evolution of both clouds from $t = 23$ to $t = 40$ Myr.

(A color version and animations of this figure are available in the online journal.)

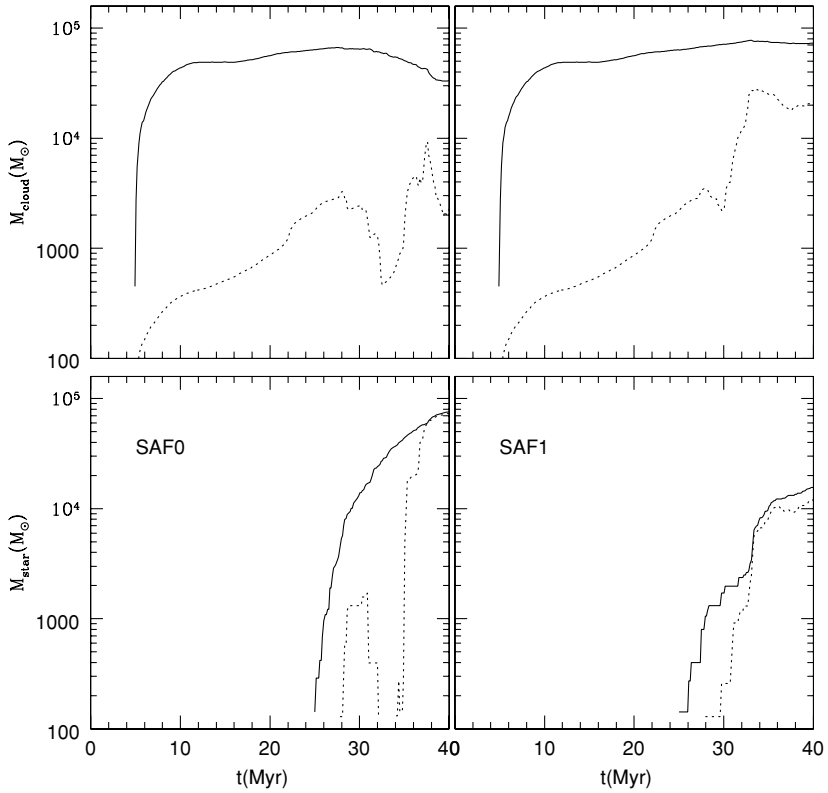

Figure 5. Evolution of the dense ($n \geqslant 100$ cm^{-3}) gas mass (top panels) and the stellar mass (bottom panels) for the SA simulations, without (left panels, run SAF0) and with (right panels, run SAF1) feedback. The solid lines refer to the total (dense gas or stellar) masses in the computational box, while the dotted lines refer to the masses in a cylinder with length and diameter of 10 pc with its axis along the x-direction, centered in the middle of the computational box, which contains the dense gas making up the cloud. The dense gas mass in both the full computational box and in the central cylinder is seen to increase upon the inclusion of feedback.

Central Cloud has grown to a mass of nearly $3 \times 10^4\ M_\odot$ in run SAF1 (cf. Figure 5). In the case of the LA runs, because star formation occurs in a much more scattered fashion, we study two of the regions exhibiting the strongest star formation activity, neither of which is located at the center of the numerical box. These are shown in Figure 4, and we refer to them as Cloud 1 and Cloud 2.

4.2. Effect of Stellar Feedback on the SFE and on the Clouds' Evolution

Our main interest in this contribution is the effect of the feedback on the efficiency of the star formation process and the identification of the mechanism through which this effect is accomplished. Figure 5 shows the evolution of the dense gas mass (top panels) and the stellar mass (bottom panels) in these simulations, with (right panels) and without (left panels) feedback. The solid lines refer to the total masses in the computational box, while the dotted lines refer to the masses in a cylindrical region of length and diameter equal to 10 pc, centered at the center of the numerical box, containing the Central Cloud. Figures 6 and 7 show the corresponding plots for Cloud 1 and Cloud 2. Here, the solid lines represent the masses for the full simulation box, and the dotted, short-dashed, and long-dashed lines represent the masses contained in cylinders of length and

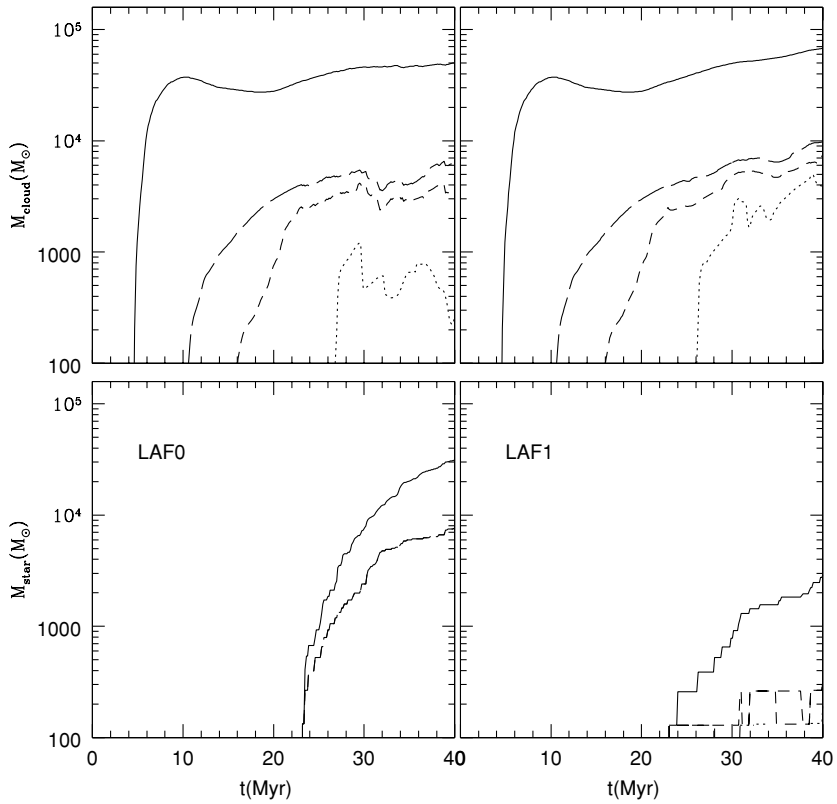

Figure 6. Evolution of the dense ($n \gtrsim 100$ cm^{-3}) gas mass (top panels) and the stellar mass (bottom panels) for Cloud 1 in the LA simulations, without (left panels) and with (right panels) feedback. The solid lines refer to the total masses (dense gas or stellar) in the computational box. The other lines refer to the masses in cylinders of length and diameter 10 pc (dotted lines), 20 pc (short-dashed lines), and 30 pc (long-dashed lines) enclosing the densest regions of the clouds. As in Figure 5, the dense gas mass in both the whole box and in the cylinders is seen to increase upon the inclusion of feedback. In the bottom left panel, the lines corresponding to the cylinders of sizes 20 and 30 pc coincide, because the stellar content in both is the same. The 10 pc cylinder contains no stellar particles.

diameter 10, 20, and 30 pc, respectively, enclosing the clouds. The locations of the cylinders are chosen by visually locating the bulk of the clouds at the initial times shown in the panels of Figure 4, taking advantage of the fact that the clouds do not move much, due to their relatively large masses. We have chosen to show three different cylinder sizes because the clouds have very complicated morphologies, with filaments that extend out over tens of parsecs and connecting with other clouds (Figure 4), thus making it virtually impossible to fully enclose the "clouds" in any given cylindrical volume.

It is seen from Figures 5–7 that the inclusion of feedback (right panels) causes the dense gas mass to be *larger* and the stellar mass to be smaller than in the case without feedback in general, even though the total cloud mass (dense gas + stars) in the simulations is nearly the same in both the cases with and without feedback (Figure 8). As a consequence, the instantaneous SFE, defined as

$$\mathrm{SFE}(t) = \frac{M_*(t)}{M_{\mathrm{dense}}(t) + M_*(t)}, \quad (3)$$

where $M_{\mathrm{dense}}(t)$ is the mass of the dense ($n \gtrsim 100$ cm^{-3}) gas in the simulation and $M_*(t)$ is the stellar mass, naturally decreases upon the inclusion of feedback in both sets of simulations (Figure 9). Note that in Equation (3) we have explicitly written out the time dependence of the quantities involved.

The SFE is seen to be reduced by a larger factor ($\sim$10×) in the case of the LA runs, in which the collapse is less focused and less massive, than in the case of the SA ones ($\sim$3×), in which the opposite is true. In addition, in Figure 10 we show the evolution of the SFE at the level of the clouds. The left panel shows the evolution of the SFE for the Central Cloud in the SA runs. The middle panels show the corresponding plots for Cloud 1 and Cloud 2 in the LAF0 run (without feedback), and the right panels show the SFEs in the LAF1 run (with feedback). Again we see a trend for the less massive cloud (Cloud 1) to suffer a greater reduction of its SFE (by a factor of $\sim$20, from $\sim$60%–90% to $\sim$3%–4%) than the more massive one (Cloud 2, by a factor of $\sim$10, from $\sim$70%–80% to $\sim$7%–8%). We discuss the possible causes for this mass-dependent effect of the feedback in Section 4.3.2.

The factor by which the SFE is reduced upon the inclusion of the feedback in the simulations is plotted versus the system's mass in Figure 11, both for the full amount of dense gas in the simulations and for each of the clouds we have been considering. We see that two sets of points are clearly defined in this plot, one for the clouds and one for the simulations. In both cases, however, the trend of a larger reduction factor at smaller dense gas mass is clearly observed, although at the level of simulations, we see that their masses are not very different. Thus, in this case the different reduction factors must include a contribution from the larger degree of fragmentation occurring in the LA simulations due to the larger amplitude of the initial turbulent fluctuations.

In order to compare the SFEs of our simulated clouds with those of real molecular clouds, it is convenient to note that regions of low-mass star formation generally have low SFEs ($\sim$1%–5%; Spezzi et al. 2008) while cluster-forming cores have SFE $\sim$30%–50% (Lada & Lada 2003). Thus, we can check whether the SFEs and SFRs of our three clouds follow the

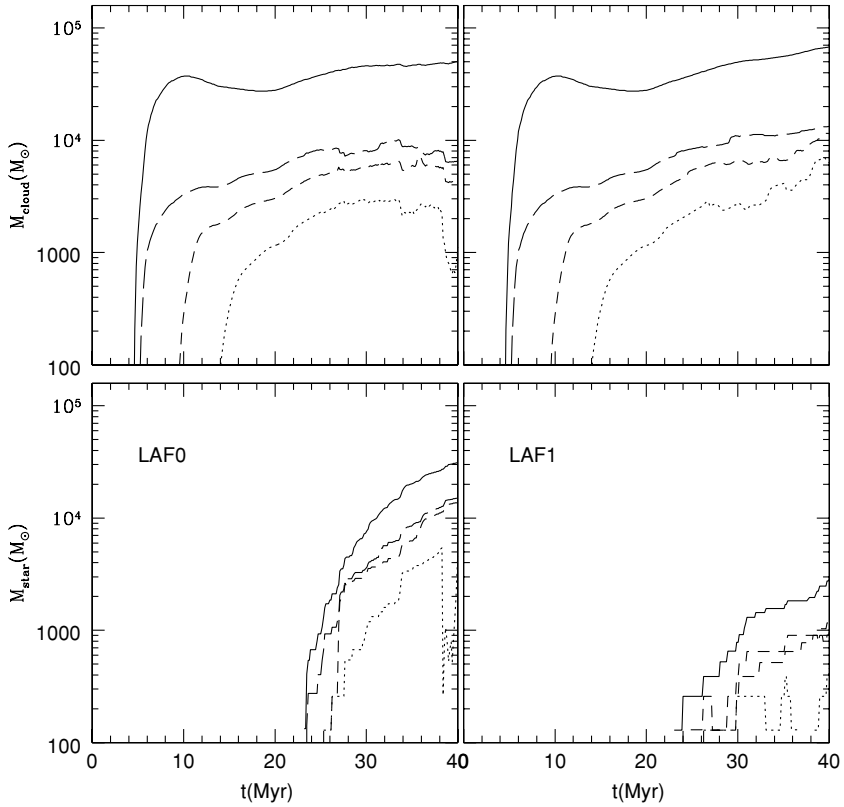

Figure 7. Evolution of the dense ($n \geqslant 100$ cm^{-3}) gas mass (top panels) and the stellar mass (bottom panels) for Cloud 2 in the LA simulations, without (left panels) and with (right panels) feedback. The solid lines refer to the total masses in the computational box. The other lines refer to the masses in cylinders of length and diameter 10 pc (dotted lines), 20 pc (short-dashed lines), and 30 pc (long-dashed lines). As in Figure 5, the dense gas mass in both the whole box and in the cylinders is seen to increase upon the inclusion of feedback.

same trend. Figure 12 shows the evolution of the SFRs for our three clouds. From these plots, we find that the average SFR of the Central Cloud starting from $t = 32$ Myr (the time at which a large, roughly stationary SFR sets in) is $\langle \mathrm{SFR} \rangle \sim 1450\, M_\odot$ Myr^{-1}, while for Clouds 1 and 2, we find $\langle \mathrm{SFR} \rangle \sim 30$ and 60 $M_\odot$ Myr^{-1} during their entire star-forming stages, respectively. From here, and using the instantaneous SFE at $t = 40$ Myr from Figure 10, we can then plot the SFE versus the SFR. This is shown in Figure 13, in which both the SFR and the SFE have been multiplied by an extra factor of 0.5, to represent the fact that the efficiency within the stellar particles, which are created at a density of $n = 4 \times 10^6$ cm^{-3} in our simulations, is still expected to be smaller than unity, since this is comparable to the density of cluster-forming cores, whose SFE is known to be ∼30%–50% (Lada & Lada 2003). We take 0.5 as a representative value.

We see that the Central Cloud has values of the SFR and the SFE comparable to those of cluster-forming cores (Lada & Lada 2003). Specifically, Vázquez-Semadeni et al. (2009) estimated an SFR $\gtrsim 250\, M_\odot$ Myr^{-1} for the Orion Nebula Cluster (ONC). This calculation used an estimated age spread of the ONC of $\lesssim$2 Myr (Hillenbrand 1997), and Tobin et al. (2009)'s result of there being 1613 stars in the ONC. Taking this number as a proxy for the total stellar production of this region and a mean stellar mass of 0.3 $M_\odot$ (Hillenbrand & Carpenter 2000), this implied a total stellar mass of ∼500 $M_\odot$. On the other hand, Krumholz & Tan (2007) quote a total stellar mass in the ONC of ∼4600 $M_\odot$ (Hillenbrand & Hartmann 1998) and an age spread of ∼3 Myr (Tan et al. 2006), implying an SFR ∼1530 $M_\odot$ Myr^{-1}. These values bracket the SFR we measured for our Central Cloud.

Concerning the SFE, Figure 13 shows that the Central Cloud has SFE ∼10%, which is comparable to that of the Orion A cloud (Carpenter 2000), in which the OMC-1 clump is contained. Thus, our Central Cloud may be compared to the Orion A cloud, and its dense core, discussed in Vázquez-Semadeni et al. (2009), is comparable to the OMC-1 clump.

On the other hand, Clouds 1 and 2 are seen in Figure 13 to have SFRs comparable to those of low-mass star-forming clouds, ∼10–100 $M_\odot$ Myr^{-1}, such as Taurus, Cha II, or Lupus, in which the SFE is known to be ∼1%–4% (Spezzi et al. 2008). Although these efficiencies compare very well with the SFEs we report for Clouds 1 and 2, those regions do not have OB stars, and therefore lack the specific type and power of energy feedback included in our simulations. So, this comparison must be considered tentative at best at the moment. Nevertheless, the coincidence is interesting and warrants further research, considering the presence of appropriate energy sources in those star-forming regions, such as winds and outflows (Norman & Silk 1980; Li & Nakamura 2006).

4.3. The Physical Processes Acting on the Clouds

4.3.1. Cloud "Destruction"

Up to the 40 Myr time to which we have evolved our simulations, the three large clouds (the Central Cloud in run SAF1 and Clouds 1 and 2 in run LAF1) do not show any instances of the dense gas mass reversing its increasing trend and beginning to decrease due to the feedback, as can be seen in Figures 5 through 7. Apparently, the H II region-like

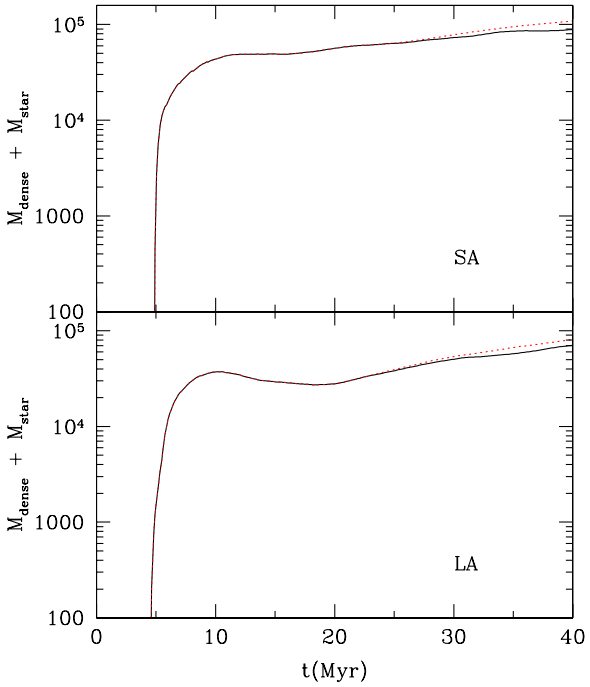

Figure 8. Evolution of the total (dense gas + stars) mass for the four simulations. The SA simulations are shown in the top panel, while the LA runs are shown in the bottom panel. The black, solid lines refer to simulations with feedback and the red, dotted lines represent runs without it. The colors are shown in the online version only.

(A color version of this figure is available in the online journal.)

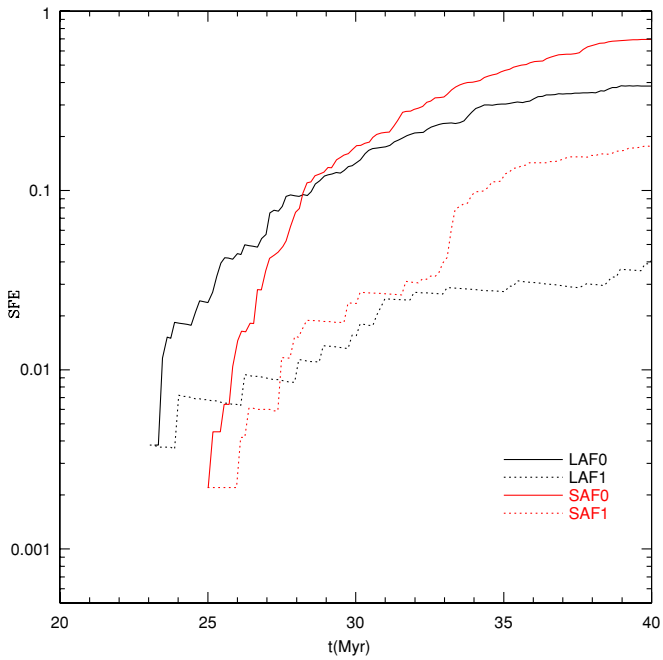

Figure 9. Evolution of the instantaneous SFE, as defined in Equation (3), in the full simulation box in the four runs.

(A color version of this figure is available in the online journal.)

feedback we use is unable to overwhelm the large gravitational potential well of these clouds and their enveloping "atomic" gas reservoirs.

Instead, complete destruction seems to be able to occur in small clumps. This can be seen in the animation corresponding to Figure 3, in which various small clumps are seen to be destroyed by their stellar products. Three particularly conspicuous ones are as follows: first, the one that forms a stellar particle at the very starting frame (record 179) of the animation, slightly above and to the right of the screen's center. Next, another stellar particle appears in the clump almost at the left border of the frame, about 2/3 of the way from bottom to top, at record 187. Finally, a third particle appears at record 189, slightly below and to the right of the screen's center, as the result of the collision of two clumps. In all of these cases, a single stellar particle is formed ($\sim$120 $M_{\odot}$), and the clump is destroyed. It is worth noting that actually, the expansion of the H II regions formed produces new clumps from the material collected around it, but these new clumps either disperse or simply do not form new stars.

Thus, we conclude, similarly to Krumholz et al. (2006), that small clouds ("clumps") are rapidly destroyed, while large clouds may survive for longer times. However, our clouds exhibit a fundamental difference with respect to the model considered by those authors, namely that the clouds are accreting in general. In the following section, we now discuss this feature.

4.3.2. Accretion Versus Feedback

One crucial feature in all our simulations is that *the clouds are accreting material from the surrounding diffuse medium.* This is fundamentally different from models in which the clouds are isolated entities, in rough balance between their self-gravity and the turbulent pressure, possibly driven by the stellar feedback. The accretion competes with star formation and stellar feedback in regulating the cloud's mass and coherence, with important consequences. First of all, this implies that simple observational estimates of the SFE in GMCs based on measuring the stellar mass and dividing it by the cloud's mass may be failing to take into account the additional "raw material" for SF contained in the part (or the whole) of the atomic envelope of the clouds that will eventually be incorporated into the GMC.

Second, the competition between feedback and accretion may explain our observation from Section 4.2 that cases with feedback are characterized by *larger* dense gas masses and smaller stellar masses than their counterparts without feedback. The smaller stellar mass is not surprising, as the obvious effect of stellar feedback is to reheat the cold, collapsing star-forming gas, thus reducing the SFR. However, the larger cold gas mass in the presence of feedback is indeed surprising, since both gas consumption by star formation and the "ionization" by stellar feedback act to reduce the dense gas mass. Our result implies that the rate of dense gas consumption by star formation far outweighs its rate of destruction by stellar feedback, so that the net effect of reducing the SFR is to allow a larger amount of dense gas to be collected by the accretion. This scenario is supported by Figure 8, which shows the total mass (dense gas + stars) in the clouds in the two sets of simulations. It is seen that the total cloud mass is nearly the same with and without feedback, suggesting that *the total cloud mass is mainly determined by the accretion, while the ratio of dense gas to stellar mass seems to be mainly determined by the feedback.*

Because the action of the feedback is very localized, it is natural to expect, however, that the total mass may be more strongly affected by the feedback when the size of the region considered is smaller. Figure 14 shows the evolution of the total mass in cylindrical regions centered in the three clouds we have been considering. It is seen that the presence of feedback causes significant fluctuations in the total mass, because both the gas and the stellar particles can often leave the counting box. Nevertheless, it is seen that in two (Cloud 2 and the

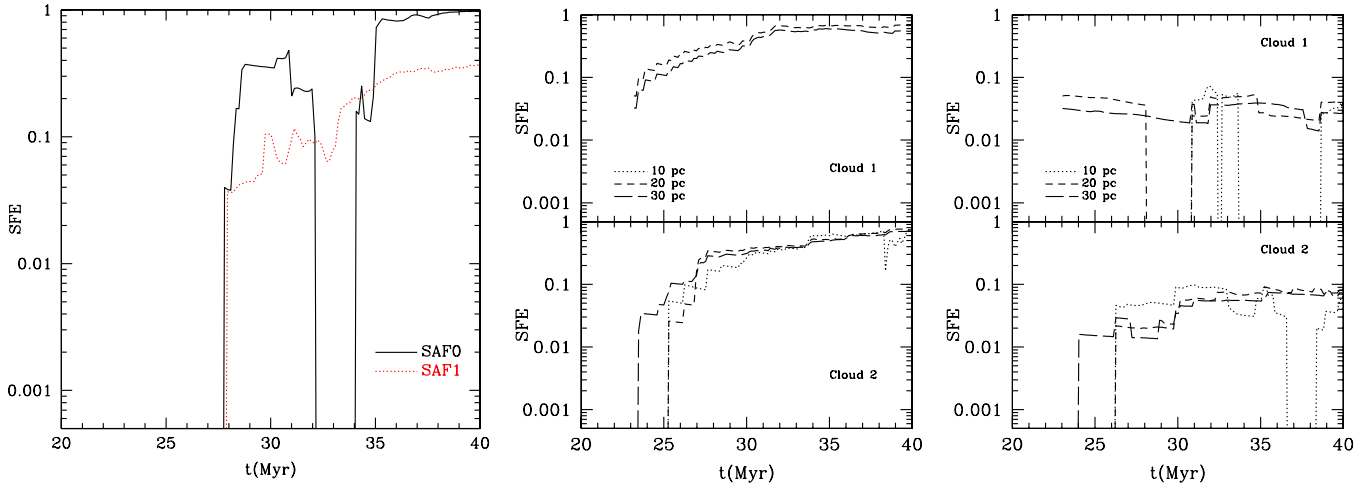

Figure 10. Evolution of the instantaneous SFE in the dense clouds in the simulations. The left panel shows the SFE for the Central Cloud of the SA runs, with and without feedback. The measurements refer to a cylindrical box with a diameter and a length of 10 pc. The middle panels show the SFE for Clouds 1 and 2 in the LAF0 simulation (without feedback), for three different cylindrical boxes, of length and diameter indicated in the labels. The gaps in the curves for the smaller cylindrical boxes correspond to times when some stellar particles migrate out of them, and no new particles have been formed. The right panels show the SFE for Clouds 1 and 2 in the LAF1 simulation (with feedback). In the middle top panel, no curve for the 10 pc cylinder is shown because there are no stellar particles within that volume in that simulation (see Figure 6).

(A color version of this figure is available in the online journal.)

Central Cloud) out of the three clouds the total mass is similar regardless of the presence of feedback, highlighting again the importance of accretion. It must be emphasized, however, that for the dense star-forming regions, the accretion consists of already dense ("molecular") gas, rather than of atomic gas from the diffuse phase, and is driven by gravity, rather than by the initial compressive flow.

It is also important to check that the tendency of the dense gas mass to increase in the presence of the feedback is not simply an artifact of the density threshold we have chosen for defining the dense gas (100 cm^{-3}), since this is very close to the post-phase transition value of the inflowing gas. Thus, this relatively low threshold might imply that we are sampling distant, non-collapsing gas that is unrelated to the gravitational contraction leading to the star formation process in the clouds, and thus not affected by the stellar feedback. To test for this, we have redone Figures 5 through 7, using a higher density threshold of 1000 cm^{-3} for defining the dense gas. We find that the results are similar for the three clouds. In Figure 15, we show the case of Cloud 2 as an illustrative example. As expected, we observe that in this case the dense gas appears later in the evolution, because large amounts of gas at densities $n > 1000$ cm^{-3} can only be formed by gravitational contraction. Nevertheless, the result that the dense gas mass *increases* rather than decreasing upon the inclusion of feedback persists. This implies that the increase of the dense gas mass upon the inclusion of feedback is an actual feature of the gas directly involved in the star formation process, and that this includes even the lower density, "atomic" envelope of the cloud.

An important conclusion from the above results is that the gas involved in the gravitational contraction leading to the star formation process extends to large scales and is not confined to the local environment of the final collapse, where the effect of the feedback is active. Moreover, besides the fact that the clouds at the largest scale are accreting material from the diffuse medium, the densest, star-forming clumps within them are accreting gas from their already dense ("molecular") environment. Thus, there appears to exist a continuous mass flux extending from the diffuse medium to the star-forming regions, in which molecular

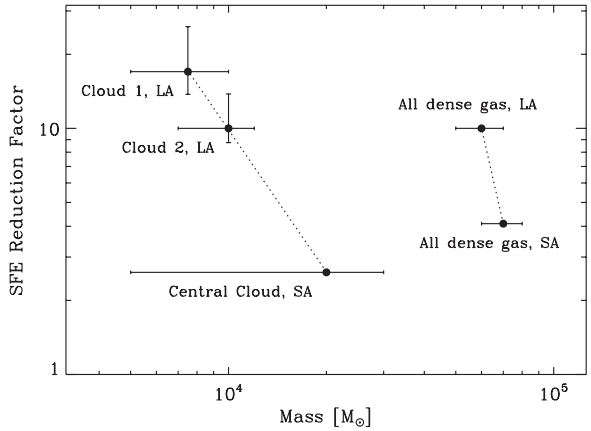

Figure 11. Reduction factor of the SFE upon inclusion of the feedback in the simulations, both for the three clouds and for the entire mass of dense gas in the simulations. The data points indicate the value of this reduction factor at $t = 40$ Myr. The masses for Clouds 1 and 2 are those measured using the 30 pc cylinders. The error bars in the masses indicate their range of fluctuation over time after their rapid initial growth phase has ended (see Figures 5–7). The error bars in the reduction factor for Clouds 1 and 2 are calculated by taking the maximum and minimum values of the ratio SFE (without feedback)/SFE (with feedback) that can be obtained using the SFE data for the three cylinder sizes of 10, 20, and 30 pc, at $t = 40$ Myr.

clouds and their cores, far from being equilibrium entities, are simply the last stages in this contraction process, which begins in post-condensation atomic gas.

Within this scenario, the significant reduction of star formation by stellar feedback is accomplished by a finely focused targeting of its action. Because it is injected by the newly formed stars, the stellar feedback acts preferentially on gas that is about to form stars next. This allows an efficient suppression of star formation, although only a modest fraction of the total available dense gas is destroyed. Presumably, a large fraction is relocated within the GMC by the feedback, slowing down the process, which may not fully terminate until the gas supply to the cloud ends, or it is completely destroyed by more powerful energy sources, such as supernova explosions.

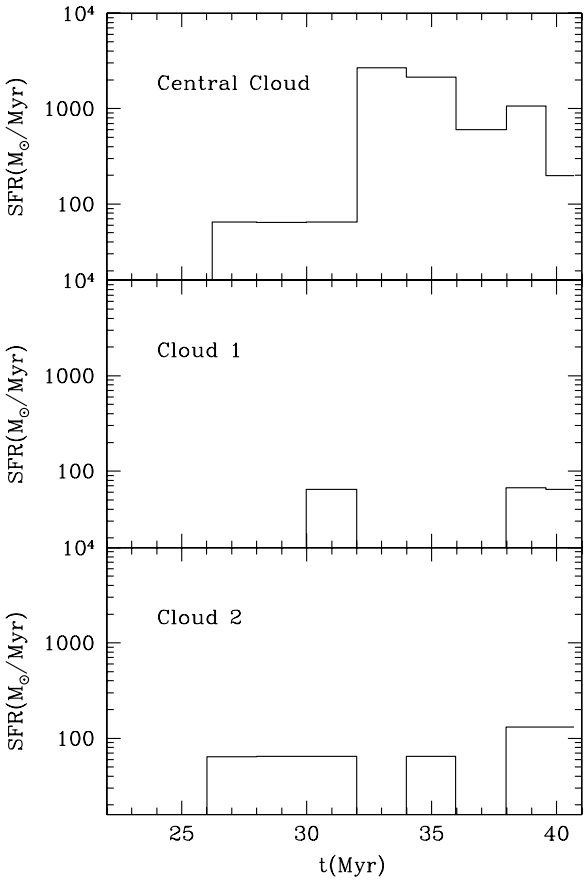

Figure 12. Evolution of the stellar particle formation rate, averaged over 2 Myr intervals, of the Central Cloud (top panel), Cloud 1 (middle panel), and Cloud 2 (bottom panel). For this plot, we only use the 10 pc cylindrical volumes for Clouds 1 and 2. Because our stellar particles form at a density of $n = 4 \times 10^6$ cm^{-3}, actual SFRs should be a factor of 2–3 lower. Gaps indicate periods over which no new stars are formed.

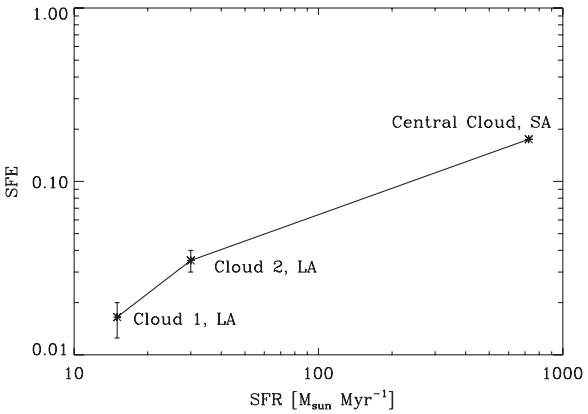

Figure 13. SFE at $t = 40$ Myr vs. the average SFR for the three clouds in the simulations, using the data from Figures 10 and 12. The error bars for the SFE for Clouds 1 and 2 indicate the range of values obtained for the SFE upon consideration of the three cylinder sizes (10, 20, and 30 pc) around the clouds. The values of both the SFR and the SFE have been multiplied by a factor of 0.5, representative of the still-lower-than-unity efficiency within our stellar particles.

This mechanism may also explain the trend observed in Section 4.2 that the SFE is more strongly reduced by the feedback in cases where the collapsing gas mass is smaller. This may be understood as a consequence of the fact that stellar feedback is localized, while the accretion is extended, and more so for greater mass of the globally gravitationally unstable region that will form the cloud. Thus, as we observe in the animation

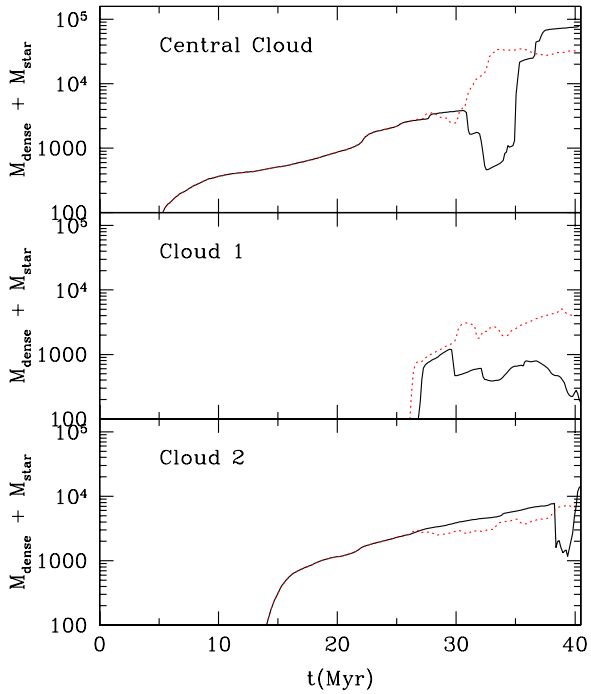

Figure 14. Evolution of the total (dense gas + stars) mass within 10 pc cylinders enclosing the three clouds in the simulations. The black, solid lines correspond to cases with feedback, and the red, dashed lines correspond to cases without feedback. The colors are shown in the online version only. It is seen that the stellar feedback is only able to significantly reduce the total mass in Cloud 1, which is the least massive of the three clouds.

(A color version of this figure is available in the online journal.)

corresponding to Figure 3, the low-mass fragments that are undergoing star formation while on their way to the central site of the global collapse in run SAF1 are easily destroyed by their stellar activity. Instead, the massive Central Cloud is not destroyed, as it continues to accrete mass from large distances at a pace that outweighs the local destruction by stellar feedback. Clouds 1 and 2 in run LAF1, which do not involve such an extended collapse, are intermediate cases, in which the clouds are not destroyed by the feedback, but the latter is more efficient in reducing the SFE. We can conclude that the efficacy of the feedback in destroying the cloud is maximal when its region of influence is comparable to the spatial extent of the infall and is progressively reduced as the latter involves progressively larger coherence lengths.

4.4. Cloud Structure

Here, we consider the global physical properties of the clouds. We postpone a discussion of the properties of individual clumps within the clouds for a future study, to be performed at higher resolution. One such study, including magnetic fields, although not including stellar feedback, has recently been presented by Banerjee et al. (2009).

4.4.1. Density Probability Density Functions

It is important to determine the physical conditions in our clouds in order to assess their degree of realism. One basic diagnostic is the probability density function (PDF) of the density field. Although it is well established that in isothermal flows the density PDF takes a lognormal form (Vázquez-Semadeni 1994; Padoan et al. 1997; Passot & Vázquez-Semadeni 1998; Nordlund & Padoan 1999; Ostriker et al. 1999, 2001;

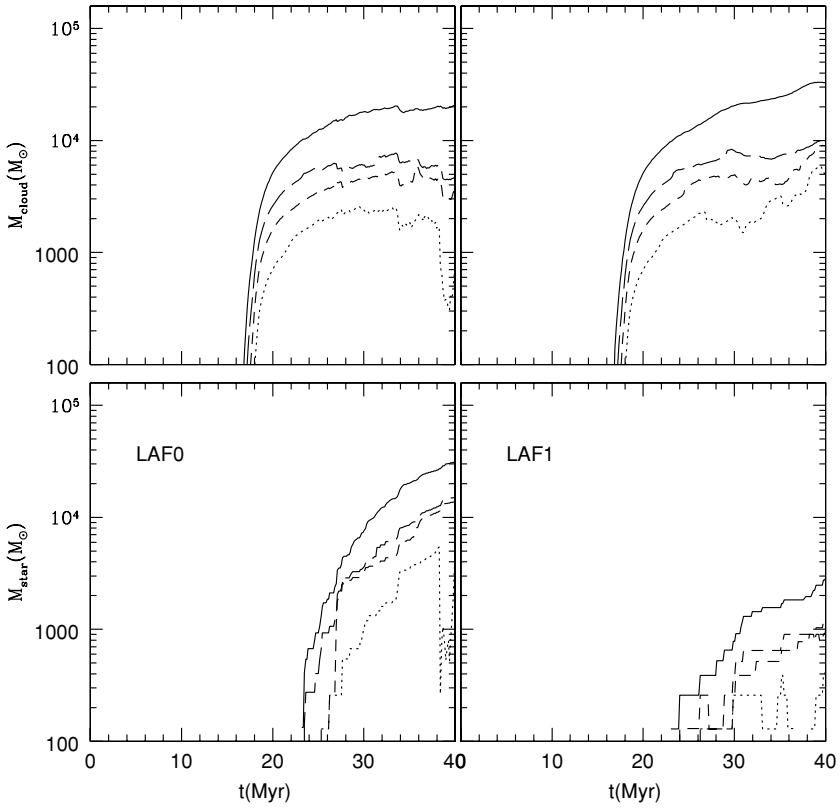

Figure 15. Same as Figure 7, but defining the dense gas as that with $n > 1000$ cm^{-3}. The dense gas appears at a later time, as it is formed by the gravitational contraction that begins several Myr earlier in the less dense, cold "atomic" phase. As in Figure 7, the dense gas mass increases upon inclusion of stellar feedback.

Federrath et al. 2008), for non-isothermal flows the expectation is in general different, with a near-power-law tail developing at high densities for flows softer than isothermal (Passot & Vázquez-Semadeni 1998; Scalo et al. 1998; Nordlund & Padoan 1999; Gazol et al. 2005; de Avillez & Breitschwerdt 2004; also see, e.g., Wada & Norman 2001, 2007), and a bimodal form arising for thermally bistable flows (Vázquez-Semadeni et al. 2000; Gazol et al. 2005; Audit & Hennebelle 2005; see also the review by Vázquez-Semadeni 2009).

Figure 16 shows the density PDFs for the whole simulation box of the SA runs (top panels) and of the LA runs (bottom panels). The right panels show the entire density range, while the left panels show the PDF for the dense gas ($n \geqslant 100$ cm^{-3}) only. The whole-range PDFs exhibit the bimodality typical of thermally bistable flows, although the high-density tail is seen to exhibit an excess over the power law in both the cases with and without feedback. This is probably due to the action of self-gravity (Klessen 2000; Dib & Burkert 2005; Vázquez-Semadeni et al. 2008). In addition, the cases with feedback show a slight excess over the cases without it at densities 10^3 cm$^{-3} \lesssim n \lesssim 10^5$ cm^{-3}, probably due to the formation of compressed regions by the expanding "H II regions." The high-density PDFs, being just the $n > 100$ cm^{-3} tail of the whole-range PDFs, only show more detail of the very high density gas, up to the star-forming density of 4×10^6 cm^{-3}, but with the same shape of the curves as in the whole-range PDFs.

In order to see the PDFs at the locations of the three main clouds we have studied (the Central Cloud in the SA runs and Clouds 1 and 2 in the LA runs), we show in Figure 17 their corresponding density PDFs. It is noteworthy that the PDFs again show a roughly power-law shape at high densities over 3–4 orders of magnitude in density, in agreement with the expectation for softer-than-isothermal flows (Passot & Vázquez-Semadeni 1998; Nordlund & Padoan 1999). This is at odds with results from numerical simulations of turbulent isothermal gas in closed boxes, but then again our clouds are *not* isothermal. They are characterized by an effective polytropic equation of state $P \propto \rho_{\rm eff}^{\gamma}$, with $\gamma_{\rm eff}$ varying from 0.8 to nearly unity for $n \gtrsim 100$ cm^{-3}, as can be seen in Figure 18. Real interstellar molecular gas is not expected to be exactly isothermal either (Scalo et al. 1998; Spaans & Silk 2000; Jappsen et al. 2005). Moreover, our clouds are not directly confined by a closed box, but rather they are immersed in a diffuse, warmer medium which, as proposed by, e.g., Li & Goldsmith (2003) and Hennebelle & Inutsuka (2006), infiltrates the clouds to some degree. Thus, the density PDFs for the volumes containing our clouds also exhibit the bimodal shape characteristic of thermally bistable flows, and have low-density tails that extend down to the warm neutral medium (WNM) regime, contrary to what happens in isothermal simulations. Note, however, that in our case, part of the warm gas originates locally by the stellar heating, rather than having entered the clouds from the outside through a turbulent boundary (Banerjee et al. 2009).

In order to quantify the amount of gas present in the regions occupied by the clouds, we show in Table 2 the mass and volume filling factors (FFs) of the diffuse ($n < 100$ cm^{-3}) and dense ($n > 100$ cm^{-3}) gas in cylinders of 10, 20, and 30 pc in length and diameter, enclosing the clouds. We see that in fact, in most cases, the dense gas occupies a relatively small fraction of the volume $\lesssim$15%, although it contains the largest fraction of the mass. This happens even in the case of the SA simulations, in which the collapse is most focused, producing a cloud that is highly centrally concentrated and well localized in space. Yet, even in this case, the largest volume FF of the dense gas

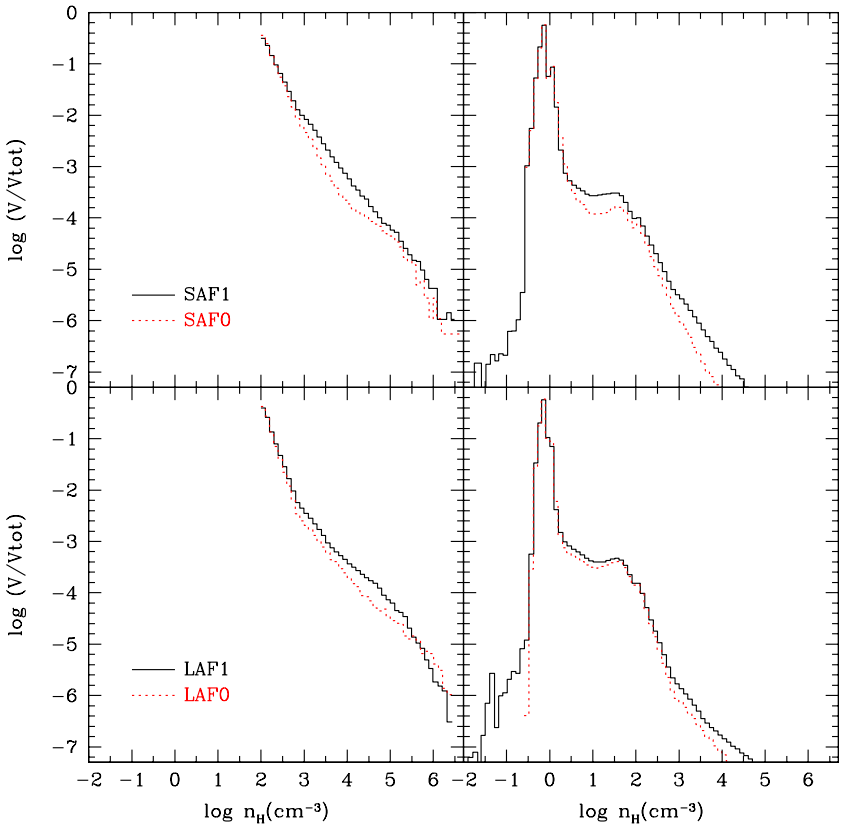

Figure 16. Density PDFs at $t = 40$ Myr for the entire simulation boxes of the SA runs (top panels) and the LA runs (bottom panels). The right panels show the PDFs for the entire range of densities, while the left panels show the PDFs of the dense gas only ($n \geqslant 100$ cm^{-3}). The red, dotted lines refer to the simulations without feedback, while the black, solid lines show represent the simulations with feedback.

(A color version of this figure is available in the online journal.)

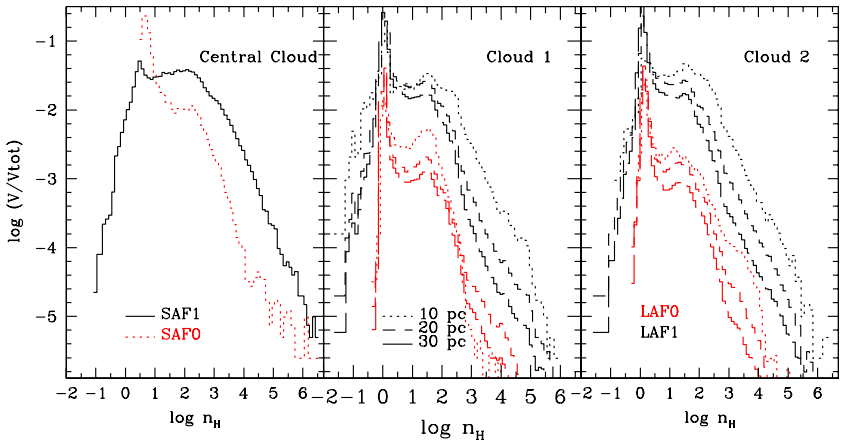

Figure 17. Density PDFs at $t = 40$ Myr for the cylindrical regions containing the three main clouds in the simulations: the Central Cloud in the SA runs (left panel), and Clouds 1 (middle panel) and 2 (right panel) in the LA runs. The PDFs for the Central Cloud region are computed in a cylinder with length and diameter equal to 10 pc, while those for Clouds 1 and 2 are computed in cylinders of length and diameter equal to 10, 20, and 30 pc. Red lines indicate cases without feedback and are displaced downward by a factor of 10 for better viewing in the cases of Clouds 1 and 2. Black lines indicate cases with feedback.

(A color version of this figure is available in the online journal.)

(f_d; occurring for the smallest cylinder) only reaches 36% (in run SAF1). Interestingly, note that f_d is *larger* in the case with feedback than in the case without, suggesting again that the feedback prevents the dense gas from being converted to stars, and thus allows it to accumulate in the region.

4.4.2. Velocity Dispersions and Virial Masses

Finally, we investigate the global velocity dispersion (Δv) in the Central Cloud and Clouds 1 and 2. This is shown in Figure 19. The solid lines show the density-weighted value, while the dotted lines show the volume-weighted value. Black lines denote cases with feedback, and red lines correspond to cases without it.

For the Central Cloud and Cloud 2, which are the two most massive ones, the density-weighted velocity dispersion, which highlights the dense gas, *decreases* upon the inclusion of feedback. Without feedback, in the Central Cloud, it reaches very high values at the end of the run ($\sim$15 km s^{-1}, corresponding

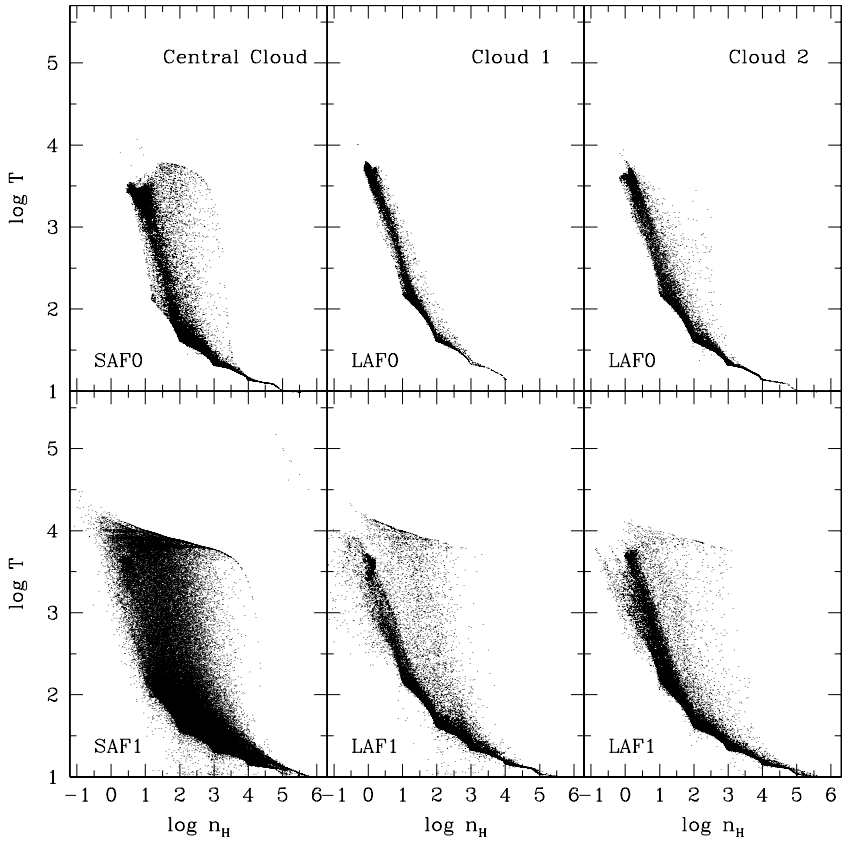

Figure 18. Phase-space diagrams of temperature vs. density for the Central Cloud (left panels), Cloud 1 (middle panels), and Cloud 2 (right panels) at $t = 40$ Myr. The top panels show the cases without feedback, and the bottom panels show the cases with feedback. It can be seen that, for most points with densities 100 cm^{-3} $< n < 10^6$ cm^{-3}, the temperature only varies between ∼10 and 40 K. The exceptions are locations recently heated by new stars.

Table 2
Mass and Volume FFs for Gas in the Clouds[a]

Model	Cyl. Length	Cloud	Mass FF		Volume FF	
	(pc)		Low Dens.	High Dens.	Low Dens.	High Dens.
SAF0	10	Central	0.04	0.96	0.92	0.08
	20		0.07	0.93	0.96	0.04
	30		0.14	0.86	0.98	0.02
SAF1	10	Central	0.02	0.98	0.64	0.36
	20		0.08	0.92	0.84	0.16
	30		0.15	0.85	0.93	0.07
LAF0	10	C1	0.27	0.73	0.90	0.10
	20		0.27	0.73	0.97	0.03
	30		0.41	0.59	0.98	0.02
	10	C2	0.12	0.88	0.90	0.10
	20		0.17	0.83	0.96	0.04
	30		0.24	0.76	0.98	0.02
LAF1	10	C1	0.17	0.83	0.83	0.17
	20		0.29	0.71	0.94	0.06
	30		0.39	0.61	0.97	0.03
	10	C2	0.09	0.91	0.83	0.17
	20		0.21	0.79	0.95	0.05
	30		0.26	0.74	0.97	0.03

Note. [a] The FFs are calculated for low-density ($n < 100$ cm^{-3}) and high-density ($n > 100$ cm^{-3}) gas in cylinders of the indicated length containing the clouds under study.

to Mach numbers $M_s \sim 50$–75), which in fact are significantly larger than typical values for cloud complexes of comparable mass ($M \gtrsim 10^4\, M_\odot$; e.g., Dame et al. 1986; Rathborne et al. 2009). Instead, in the run including feedback, Δv reaches values ∼5–6 km s^{-1} (rms Mach number, $M_s \sim 20$), in much better agreement with typically observed values. On the other hand, the volume-weighted velocity dispersion, which highlights the less dense gas, is seen in Figure 19 to *increase* upon the inclusion of feedback. In Clouds 1 and 2, which are less massive and more scattered than the Central Cloud, Δv does not achieve exceedingly large values in any case.

These results can be understood as a consequence of the fact that the dense gas acquires its largest velocities in the case of free-fall collapse. However, the collapse flow is dismantled in its final (fastest) stages by the stellar feedback, so that it is the high-velocity dense gas that is preferentially destroyed by the feedback. On the other hand, this gas becomes warm, diffuse, high-velocity *expanding* gas, which is the one highlighted by the volume weighting. These results again reinforce the notion that the feedback is mostly applied on the gas that is closest (but not quite there yet) to forming stars.

Once we have determinations of the velocity dispersion in the cylinders containing the clouds, it is natural to measure the virial mass ($M_{\rm vir}$) of the clouds and compare it with their real mass M, in order to check whether they look "virialized." We compute the virial mass through the standard formula

$$M_{\rm vir} \equiv 210 \left(\frac{R}{\rm pc}\right) \left(\frac{\Delta v}{\rm km\ s^{-1}}\right)^2 M_\odot, \qquad (4)$$

(see, e.g., Caselli et al. 2002; Tachihara et al. 2002; Klessen et al. 2005). For the real cloud mass we consider the sum of the gas (dense + diffuse) and stellar masses in the volume being

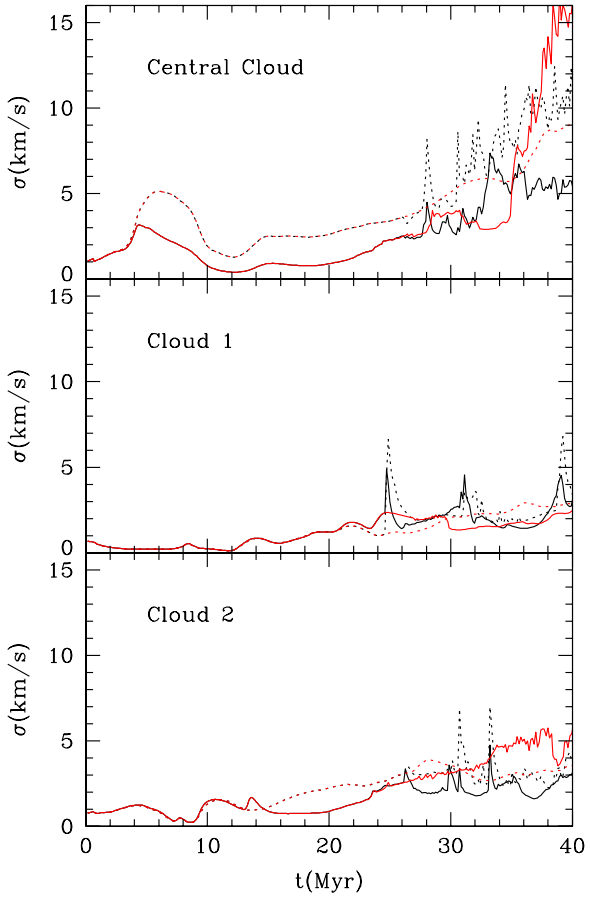

Figure 19. Evolution of the velocity dispersion σ in the three clouds. The solid lines show the density-weighted value, while the dotted lines show the volume-weighted value. Red lines correspond to cases without feedback and black lines correspond to cases with feedback.

(A color version of this figure is available in the online journal.)

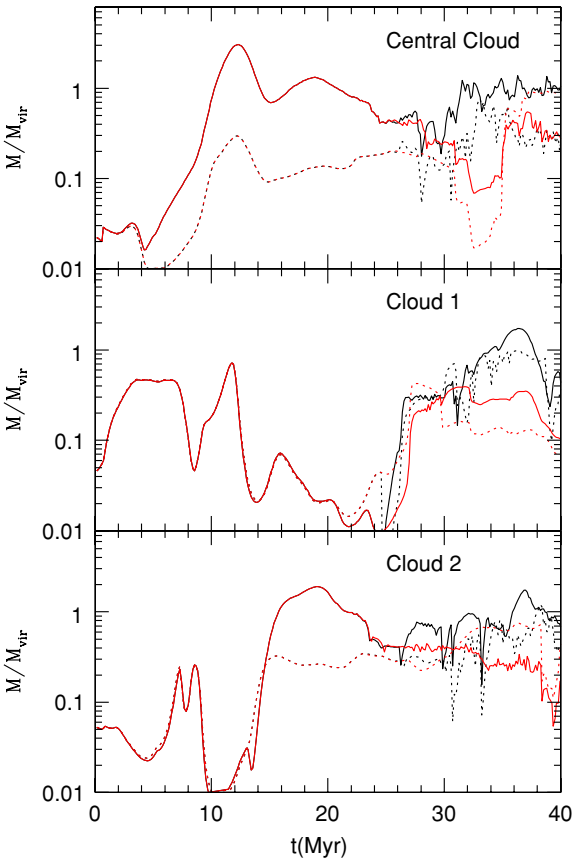

Figure 20. Evolution of the ratio of actual to virial mass for the three clouds. Red lines correspond to the runs without feedback. Black lines correspond to the runs with feedback. Solid lines correspond to the density-weighted velocity dispersion, while dotted lines correspond to the volume-weighted one.

(A color version of this figure is available in the online journal.)

considered. It is important to note that, with this prescription, variations in the value of the ratio come exclusively from the estimate of the virial mass, because it *does* depend on the weighting used, while the actual cloud mass is independent of the method of weighting.

Figure 20 shows the evolution of the ratio $M/M_{\rm vir}$ for the three clouds, showing the cases with and without feedback, and using volume and density weighting for the calculation of Δv. In all cases, we observe that, at advanced stages of the evolution, when the clouds have been fully assembled ($t \gtrsim 25$ Myr), this ratio is closest to unity when feedback is included and density weighting is used in the calculation of Δv. The cases with no feedback and density weighting are systematically lower than unity by factors of ∼2–10. The cases with volume weighting are more strongly fluctuating, but it is noteworthy that the ratio often takes values close to unity anyway.

From these results, we conclude that, in the case with feedback, the clouds appear to be in a pseudo-virialized state with respect to the velocity dispersion of the dense gas (highlighted by the density weighting). In this state, there is an approximate force balance between self-gravity and feedback driving. However, it differs from true virialization because of the presence of mass sources (the accretion from the diffuse environment) and sinks (the consumption by star formation and the destruction by stellar feedback) in the system. These seem to self-regulate, so as to be capable of maintaining an approximately constant cloud mass while accretion persists. On the other hand, when the velocity dispersion of the warm gas is taken into account (still in the case with feedback), the clouds appear to be slightly sub-virial, suggesting that the newly formed warm gas in the H II regions is capable of escaping the cloud.

In the cases without feedback, the clouds also appear to be sub-virial even with respect to the density-weighted virial mass estimate. In this case, this appears to be a consequence of the dense gas being in free-fall collapse and into a potential well produced not only by its own self-gravity, but also by the previously formed stars that have fallen there too (see Vázquez-Semadeni et al. 2009).

5. CAVEATS AND LIMITATIONS

Of course, our simulations are not free of caveats and limitations. Two that stand out are the resolution and the nature of the feedback that we have included. Concerning the resolution, in this paper we have used a relatively limited one, in order to speed up the simulations, at the expense of not fulfilling the Jeans criterion proposed by Truelove et al. (1997). However, as explained in Section 2.3, we do not consider this a problem for our study, since we have restricted it to the global properties of the clouds, rather than their detailed structure, and we have avoided addressing issues related to the fragmentation of the final stages of collapse in the clouds, such as the mass distribution of the cores and stellar products. We plan to perform a higher-resolution study in a forthcoming paper, in which we can address these issues.

The second limitation is the nature of the stellar feedback that we have considered, which in this study has been restricted to local heating representing the ionizing radiation from massive stars, similarly to the approach used by, e.g., Yorke et al. (1982), Vazquez-Semadeni et al. (1995), and Passot et al. (1995), neglecting other sources such as outflows from stars of all masses (e.g., Norman & Silk 1980; Li & Nakamura 2006; Matzner 2007; Nakamura & Li 2007; Carroll et al. 2009; Wang et al. 2010). We do this in part for the numerical simplicity of the approach, and in part because here we have been mainly interested in the SFE and cloud evolution at the scale of GMCs, for which the expansion of H II regions is likely the main driver (Matzner 2002). However, the neglect of bipolar outflows may introduce a non-negligible bias in our finding that smaller-scale clumps are destroyed by the feedback, and this should be confirmed by future simulations that can better resolve these objects and include bipolar outflows.

6. SUMMARY AND CONCLUSIONS

In this paper, we have presented a numerical investigation of the evolution of dense ("molecular") clouds, starting from their formation by transonic compressions in the WNM, followed by a phase transition to the cold neutral medium, the onset of gravitational collapse, star formation, and, finally, energy feedback from massive-star ionizing radiation and the formation of expanding H II regions.

A crucial difference between the results from our simulations and other models, and theories of the self-regulation of star formation and its efficiency (e.g., Whitworth 1979; Elmegreen 1983; Franco et al. 1994; McKee & Tan 2003; Krumholz & McKee 2005) is that the clouds in our simulations are in general accreting material at high rates from the surrounding diffuse medium, rather than having a fixed mass. This implies that *the material making up a cloud is constantly being replenished over time* because, on the one hand it is accreting fresh gas, and on the other it is losing mass to star formation and stellar ionization. The star-forming regions can be considered to be not objects, but rather the *loci* where the gas is just "passing through," from the diffuse-gas state to the "star" state, similarly to the nature of a flame, which is the locus of the gas undergoing combustion in a candle, with fresh air entering at its base, burning while it transits through the flame, and the exhaust gases leaving at the top. This scenario is consistent with recent proposals that the line widths observed in molecular clouds and their substructures amount essentially to a gravitationally driven mass cascade (Field et al. 2008). Within this framework, the clouds attain a nearly stationary state, but in which the near constancy of the clouds' mass is not so much due to internal support, but rather due to the continuous replenishment from the atomic environment. Furthermore, the scenario repeats itself at smaller scales, with star-forming regions accreting gas from more distant and diffuse regions within their parent molecular clouds.

In this context, we have found that the SFE in the clouds is readily decreased by feedback to levels consistent with observational determinations *at all times during the clouds' evolution* up to the maximum integration time of 40 Myr that we have considered. This is a significant improvement over our previous non-magnetic studies of the SFE in the context of cloud evolution without feedback, in which the SFE at late times is often found to be excessive (e.g., Vázquez-Semadeni et al. 2007; Rosas-Guevara et al. 2010). However, we have found that the reduction factor upon the inclusion of feedback is an inverse function of the dense gas mass in the system and of the degree of coherence of the global collapse, as illustrated in Figure 11. This result is complemented by the additional observation that low-mass clumps are fully destroyed by the feedback. Together they imply that at some point, below a certain critical collapsing mass, the appearance of a stationary state may not occur anymore. This is in qualitative agreement with the results of Krumholz et al. (2006), although their model does not include mass accretion onto the cloud. We plan to present one such model in a future paper.

In general, our results may provide an explanation for the observational fact that regions of massive-star formation, which are themselves more massive than regions of low-mass star formation, appear to have higher SFEs (Lada & Lada 2003) than regions forming low- and intermediate-mass stars (Evans et al. 2009). Essentially, our results imply that *the more massive the region, the less effective the feedback is in reducing the SFE.* Specifically, these results indicate that the role of the feedback is not the same in all clouds, but rather depends on the initial conditions of the large-scale collapse that produces each individual region. Regions in which the amount of mass involved in the collapse overwhelms the destructive action of the feedback may reach a stationary state that appears virialized, but in which there is actually a continuous processing of material, since on the one hand the cloud is accreting mass from the outer infalling material, and on the other hand it is losing mass through consumption by star formation and evaporation by the feedback. In this case, termination of the star formation episode probably requires the termination of the gas reservoir involved in the global collapse and is independent of the feedback. However, this need not be in contradiction with the low observed global efficiency of star formation, if only a small fraction of a GMC's mass is involved in the collapse at any moment in time, with the rest being either supported (by, e.g., the magnetic field), or in the process of dispersal (Elmegreen 2007). Alternatively, the star formation episode may be terminated upon the initiation of supernova events, which we have not included in the present study.

An additional consequence of the mechanisms described in this paper is that the most massive clouds appear to actually contain more mass when feedback is included than when it is not. This suggests that, first, unimpeded star formation is more efficient at removing mass from the dense gas phase to deposit into stars than the evaporation of dense gas by the stellar feedback, so that, when the latter inhibits star formation, the accretion onto the cloud accumulates larger amounts of dense gas than otherwise. Second, this indicates that the deposition of the feedback energy into the clouds is accurately targeted to gas that is already on the verge of forming stars. If this gas is a minor fraction of the total dense gas in a cloud (i.e., star formation is a highly spatially intermittent phenomenon in molecular clouds; Vázquez-Semadeni et al. 2009), then its destruction is a highly efficient way to reduce the SFE without destroying a large fraction of the cloud.

Finally, we have also investigated the density PDF in the volumes containing the clouds in our simulations, finding that in general they retain the bimodal shape characteristic of thermally bistable flows. The PDF of the dense gas exclusively shows no turnover at low densities, indicating that low densities are most abundant. The high-density tails of the PDFs have power-law shapes, as expected for softer-than-isothermal flows, although this last result may be biased by our usage of a single cooling law appropriate for atomic gas, and extrapolating it to molecular gas densities, rather than using a specific molecular cooling law. We expect to address this shortcoming in future works.

We are grateful to A. Kravtsov for providing us with the numerical code and to N. Gnedin for providing us with the useful analysis and graphics package IFRIT. The calculations were performed on the 8-core server at CRyA-UNAM, acquired through UNAM-PAPIIT grant IN112806 to P.C. This work has received partial financial support from CONACYT grants U47366-F to E.V.-S. and J50402-F to G.C.G., and UNAM-PAPIIT IN106809 to G.C.G.

REFERENCES

Audit, E., & Hennebelle, P. 2005, A&A, 433, 1
Ballesteros-Paredes, J., Klessen, R. S., Mac Low, M.-M., & Vazquez-Semadeni, E. 2007, Protostars and Planets V, ed. V, B. Reipurth, D. Jewitt, & K. Keil (Tucson, AZ: Univ. Arizona Press), 63
Banerjee, R., Vázquez-Semadeni, E., Hennebelle, P., & Klessen, R. S. 2009, MNRAS, 398, 1082
Brunt, C. M. 2003, ApJ, 583, 280
Brunt, C. M., Heyer, M. H., & Mac Low, M.-M. 2009, A&A, 504, 883
Carpenter, J. M. 2000, AJ, 120, 3139
Carroll, J. J., Frank, A., Blackman, E. G., Cunningham, A. J., & Quillen, A. C. 2009, ApJ, 695, 1376
Caselli, P., Benson, P. J., Myers, P. C., & Tafalla, M. 2002, ApJ, 572, 238
Ceverino, D., & Klypin, A. 2009, ApJ, 695, 292
Dame, T. M., Elmegreen, B. G., Cohen, R. S., & Thaddeus, P. 1986, ApJ, 305, 892
de Avillez, M. A., & Breitschwerdt, D. 2004, A&A, 425, 899
Diaz-Miller, R. I., Franco, J., & Shore, S. N. 1998, ApJ, 501, 192
Dib, S., & Burkert, A. 2005, ApJ, 630, 238
Elmegreen, B. G. 1983, MNRAS, 203, 1011
Elmegreen, B. G. 2007, ApJ, 668, 1064
Evans, N. J., et al. 2009, ApJS, 181, 321
Federrath, C., Klessen, R. S., & Schmidt, W. 2008, ApJ, 688, L79
Field, G. B., Blackman, E. G., & Keto, E. R. 2008, MNRAS, 385, 181
Franco, J., Shore, S. N., & Tenorio-Tagle, G. 1994, ApJ, 436, 795
Gazol, A., Vázquez-Semadeni, E., & Kim, J. 2005, ApJ, 630, 911
Goldreich, P., & Kwan, J. 1974, ApJ, 189, 441
Hartmann, L., Ballesteros-Paredes, J., & Bergin, E. A. 2001, ApJ, 562, 852
Hartmann, L., & Burkert, A. 2007, ApJ, 654, 988
Heitsch, F., Burkert, A., Hartmann, L., Slyz, A. D., & Devriendt, J. E. G. 2005, ApJ, 633, L113
Heitsch, F., Slyz, A., Devriendt, J., Hartmann, L., & Burkert, A. 2006, ApJ, 648, 1052
Hennebelle, P., & Audit, E. 2007, A&A, 465, 431
Hennebelle, P., & Inutsuka, S.-I. 2006, ApJ, 647, 404
Hennebelle, P., & Pérault, M. 1999, A&A, 351, 309
Heyer, M., & Brunt, C. 2007, in IAU Symp. 237, Triggered Star Formation in a Turbulent ISM, ed. B. G. Elmegreen & J. Palouš (Cambridge: Cambridge Univ. Press), 9
Hillenbrand, L. A. 1997, AJ, 113, 1733
Hillenbrand, L. A., & Carpenter, J. M. 2000, ApJ, 540, 236
Hillenbrand, L. A., & Hartmann, L. W. 1998, ApJ, 492, 540
Jappsen, A.-K., Klessen, R. S., Larson, R. B., Li, Y., & Mac Low, M.-M. 2005, A&A, 435, 611
Klessen, R. S. 2000, ApJ, 535, 869
Klessen, R. S., Ballesteros-Paredes, J., Vázquez-Semadeni, E., & Durán-Rojas, C. 2005, ApJ, 620, 786
Klessen, R. S., Heitsch, F., & MacLow, M. M. 2000, ApJ, 535, 887
Koyama, H., & Inutsuka, S.-I. 2000, ApJ, 532, 980
Koyama, H., & Inutsuka, S.-I. 2002, ApJ, 564, L97
Kravtsov, A. V. 2003, ApJ, 590, L1
Kravtsov, A. V., Klypin, A. A., & Khokhlov, A. M. 1997, ApJS, 111, 73
Krumholz, M. R., Matzner, C. D., & McKee, C. F. 2006, ApJ, 653, 361
Krumholz, M. R., & McKee, C. F. 2005, ApJ, 630, 250
Krumholz, M. R., & Tan, J. C. 2007, ApJ, 654, 304
Lada, C. J., & Lada, E. A. 2003, ARA&A, 41, 57
Li, D., & Goldsmith, P. F. 2003, ApJ, 585, 823
Li, Z.-Y., & Nakamura, F. 2006, ApJ, 640, L187
Mac Low, M.-M., & Klessen, R. S. 2004, Rev. Mod. Phys., 76, 125
Matzner, C. D. 2002, ApJ, 566, 302
Matzner, C. D. 2007, ApJ, 659, 1394
McKee, C. F., & Tan, J. C. 2003, ApJ, 585, 850
Myers, P. C., Dame, T. M., Thaddeus, P., Cohen, R. S., Silverberg, R. F., Dwek, E., & Hauser, M. G. 1986, ApJ, 301, 398
Nakamura, F., & Li, Z.-Y. 2007, ApJ, 662, 395
Nordlund, Å. K., & Padoan, P. 1999, in Proc. 2nd Guillermo Haro Conf., Interstellar Turbulence, ed. J. Franco & A. Carraminana (Cambridge: Cambridge Univ. Press), 218
Norman, C., & Silk, J. 1980, ApJ, 238, 158
Ossenkopf, V., & Mac Low, M.-M. 2002, A&A, 390, 307
Ostriker, E. C., Gammie, C. F., & Stone, J. M. 1999, ApJ, 513, 259
Ostriker, E. C., Stone, J. M., & Gammie, C. F. 2001, ApJ, 546, 980
Padoan, P., Juvela, M., Kritsuk, A. G., & Norman, M. L. 2009, ApJ, 707, L153
Padoan, P., Nordlund, A., & Jones, B. J. T. 1997, MNRAS, 288, 145
Passot, T., & Vázquez-Semadeni, E. 1998, Phys. Rev. E, 58, 4501
Passot, T., Vázquez-Semadeni, E., & Pouquet, A. 1995, ApJ, 455, 536
Peretto, N., Hennebelle, P., & André, P. 2007, A&A, 464, 983
Rathborne, J. M., Johnson, A. M., Jackson, J. M., Shah, R. Y., & Simon, R. 2009, ApJS, 182, 131
Rosas-Guevara, Y., Vázquez-Semadeni, E., Gómez, G. C., & Jappsen, A.-K. 2010, MNRAS, in press (arXiv:0911.1795)
Scalo, J., Vázquez-Semadeni, E., Chappell, D., & Passot, T. 1998, ApJ, 504, 835
Spaans, M., & Silk, J. 2000, ApJ, 538, 115
Spezzi, L., et al. 2008, ApJ, 680, 1295
Tachihara, K., Onishi, T., Mizuno, A., & Fukui, Y. 2002, A&A, 385, 909
Tan, J. C., Krumholz, M. R., & McKee, C. F. 2006, ApJ, 641, L121
Tobin, J. J., Hartmann, L., Furesz, G., Mateo, M., & Megeath, S. T. 2009, ApJ, 697, 1103
Truelove, J. K., Klein, R. I., McKee, C. F., Holliman, J. H., II, Howell, L. H., & Greenough, J. A. 1997, ApJ, 489, L179
Vázquez-Semadeni, E. 1994, ApJ, 423, 681
Vázquez-Semadeni, E. 2009, in The Role of Disk–Halo Interaction in Galaxy Evolution: Outflow vs. Infall? (arXiv:0902.0820)
Vázquez-Semadeni, E., Ballesteros-Paredes, J., & Klessen, R. S. 2003, ApJ, 585, L131
Vázquez-Semadeni, E., Gazol, A., & Scalo, J. 2000, ApJ, 540, 271
Vázquez-Semadeni, E., Gómez, G. C., Jappsen, A. K., Ballesteros-Paredes, J., González, R. F., & Klessen, R. S. 2007, ApJ, 657, 870 (Paper I)
Vázquez-Semadeni, E., Gómez, G. C., Jappsen, A.-K., Ballesteros-Paredes, J., & Klessen, R. S. 2009, ApJ, 707, 1023
Vázquez-Semadeni, E., González, R. F., Ballesteros-Paredes, J., Gazol, A., & Kim, J. 2008, MNRAS, 390, 769
Vazquez-Semadeni, E., Passot, T., & Pouquet, A. 1995, ApJ, 441, 702
Vázquez-Semadeni, E., Ryu, D., Passot, T., González, R. F., & Gazol, A. 2006, ApJ, 643, 245
Wada, K., & Norman, C. A. 2001, ApJ, 547, 172
Wada, K., & Norman, C. A. 2007, ApJ, 660, 276
Wang, P., Li, Z.-Y., Abel, T., & Nakamura, F. 2010, ApJ, 709, 27
Whitworth, A. 1979, MNRAS, 186, 59
Williams, J. P., & McKee, C. F. 1997, ApJ, 476, 166
Yorke, H. W., Bodenheimer, P., & Tenorio-Tagle, G. 1982, A&A, 108, 25
Zuckerman, B., & Evans, N. J. 1974, ApJ, 192, L149
Zuckerman, B., & Palmer, P. 1974, ARA&A, 12, 279